



Effect of antimony additions on the microstructure and performance of Zn–Mg–Al alloy coatings



Daniel A. Britton¹✉, David Penney¹, Amar D. Malla¹, Shahin Mehraban¹, James Sullivan¹, Mathew Goldsworthy¹, James McGettrick¹, Richard Johnston¹, Ria L. Mitchell² & Clive Challinor³

Microscopy, electrochemical techniques and mechanical testing are used to investigate the effect of varying antimony additions (0.45–1.8 wt%) on the microstructure and corrosion properties of zinc-magnesium-aluminium coating alloys. Samples were produced by splat casting to produce high cooling rates similar to those seen in a continuous galvanising line. X-Ray Microscopy reveals that the Sb additions produce disk-shaped Mg_3Sb_2 intermetallics, subsequently reducing or eliminating the MgZn_2 eutectic. Electrochemical testing in 1 wt% NaCl shows that the Mg_3Sb_2 phase is cathodic with respect to the bulk alloy with slower oxygen reduction kinetics. The decrease in eutectic content leads to less intense anodic activity. The combined effect is anodic and cathodic deactivation, which leads to a 43% reduction in corrosion rate as measured through LPR compared to the base alloy. This work shows that quaternary additions to ZMA coating alloys can be a potential route to improved corrosion resistance for galvanic protection.

Galvanising is regularly used to protect steel from corrosion. It is the process of applying a thin layer of zinc (Zn) onto a steel substrate by dipping the steel into a bath of liquid Zn. This can be a continuous or batch process. The Zn acts as a sacrificial anode and corrodes preferentially to the steel substrate beneath, allowing structural integrity to be maintained¹. Elemental additions can enhance properties for use in particular conditions, such as 5 wt% Al, known as Galfan and 55 wt% aluminium (Al) remainder Zn, that give increased ductility and good cut-edge protection, respectively^{2,3}. Since the early 2000's, the addition of magnesium (Mg) and Al has been used (typically both below 11 wt%) to increase corrosion protection at lower coating weights and to decrease pressing tool pollution, which leads to a reduction in manufacturing downtime and therefore lower costs⁴. The use of further additions have also been investigated as a way of enhancing the properties of steel coatings, both in traditional galvanising (GI) and ZMA galvanising^{5,6}.

Zn–Mg–Al (ZMA) alloys consist of a primary Zn dendritic structure surrounded by a binary and ternary-eutectic lamella phase. The binary eutectic typically contains Zn–MgZn₂ and the ternary comprises of MgZn₂, Zn and Al rich nodules^{7–10}. Current applications for ZMA coatings include building ventilation systems, solar panel installations and automotive parts. With a drive towards lighter and more reliable vehicles with longer lifespans, automotive manufacturers have shown increased interest in the use of ZMA-coated steels for car body panels to take advantage of the reported benefits of lower coating weights without sacrificing corrosion resistance¹¹.

However, the current challenge is unpredictable surface quality caused in part by the complex microstructure that is heavily influenced by processing parameters¹².

Previous research has shown the brittle MgZn_2 intermetallic that forms as part of the binary eutectic phase can cause the coating to crack during bending and cause a range of surface finish defects¹³. Exposure of the steel substrate to an electrolyte acts as a cathodic driving force for corrosion, causing accelerated dissolution of the Zn coating. Additionally, penetration of electrolyte into coating cracks may cause organic coatings to delaminate or suffer from filiform corrosion¹⁴.

While the presence of Mg is responsible for the formation of the brittle binary eutectic, it cannot be simply removed from the alloy as its presence heavily contributes to the improved corrosion resistance seen in ZMA alloys. MgZn_2 is attacked preferentially within the microstructure due to its lower potential, releasing Mg^{2+} ions into the system. Since Mg^{2+} is not likely to hydrolyse, the electrolyte pH may rise to levels where Zn based corrosion products are stabilised¹⁵ resulting in greater protection than traditional GI coatings. Previous work aimed at improving corrosion resistance of ZMA showed the addition of 1.8 wt% germanium (Ge) led to a decrease in the volume percentage of eutectic from 32 to 7%¹⁶. This reduces the amount of brittle, MgZn_2 phase in the final microstructure, leading to an expected rise in formability. Despite the decrease in eutectic, the alloy also showed marked improvements in corrosion performance with a 58% drop in corrosion-

¹Department of Materials, Swansea University, Swansea, UK. ²ZEISS Research Microscopy Solutions, Cambridge, UK. ³TATA Steel, Port Talbot, UK.

✉ e-mail: d.a.britton@swansea.ac.uk

induced mass loss. This was caused by the galvanic attack of Mg_2Ge , which act as ‘smart release’ inhibitors. Despite these results however, Ge is an expensive element and not commercially viable for continuous GI.

Here, the use of antimony (Sb) as an alloying addition to ZMA coatings is investigated. Sb is well known in the galvanising industry¹⁷ and has long been used as a spangle former in GI coatings.

These coatings typically contain less than 0.2 wt% Al in Zn supersaturated with Fe. The Sb lowers the surface tension and promotes large spangles synonymous with galvanised coatings. It also increases the fluidity of the bath, helping to improve surface finish¹. There has been little research into the effect of Sb additions to ZMA coatings. In this paper, the changes to microstructure and corrosion resistance of Sb containing ZMA coatings will be investigated.

Results

Microstructure characterisation

The microstructures of all four samples are compared in Fig. 1. ZMA-0Sb and ZMA-0.5Sb showed an irregular structure of primary Zn dendrites, surrounded by small amounts of binary and ternary eutectic phase shown by the light and dark grey colours, respectively. A small amount of Mg_3Sb_2 intermetallics, approximately 8.5 μm long can be seen towards the right of the image for ZMA-0.5Sb. The microstructure of ZMA-1Sb consisted of much smaller Zn dendrites, the growth of which may have been constricted by the Mg_3Sb_2 intermetallics. ZMA-2Sb showed a refined primary zinc phase and no binary eutectic phase. There was a larger number of Mg_3Sb_2 intermetallics that appeared greater in length and width compared to samples with lower additions of Sb. A summary of the microstructural effects is shown in Table 1.

The microstructure and phase morphology were investigated using imaging techniques and DSC. Figure 2a shows the microstructure of ZMA-1Sb and the typical microstructure achieved by adding Sb to ZMA alloys. Primary Zn dendrites could be seen throughout the structure, interlaced with high aspect ratio rod-shaped intermetallics of Mg_3Sb_2 . They did not appear to intersect any primary phase suggesting they were the first to freeze when the material was cast. This is consistent with the Mg-Sb phase diagram that shows Mg_3Sb_2 has a melting point of 1245 °C^{18–20}. The binary eutectic (highlighted in orange via false colour imaging) and ternary eutectic phases (highlighted in green) appear to be distributed unevenly throughout the

structure and link together many of the Zn dendrites between them. Figure 2b–e shows the original EDX maps.

The addition of Sb in each sample and individual phase area percentages of the alloys produced are given in Table 2. The area percentage of Mg_3Sb_2 increased with a rise in Sb additions to a total surface area of 4.8% in the ZMA-2Sb sample. Ternary eutectic remained relatively constant, with a range between a minimum of 20.8% in ZMA-1Sb and the maximum of 24.2% in ZMA-0Sb. Zn dendrite area increased as Sb was added, from 56.2 to 71.4% in the ZMA-0Sb and ZMA-2Sb samples, respectively. The change in binary eutectic phase area gave the most interesting results, decreasing from 13.8% in ZMA-0Sb to 4.4% in ZMA-1Sb. Furthermore, the binary eutectic phase was not detected at all in the ZMA-2Sb alloy.

DSC curves for ZMA-0Sb and ZMA-2Sb are presented in Fig. 3 and show the difference in phase formation between the two samples. Upon cooling (shown along the x-axis), exothermic releases in energy are seen at various temperatures, resulting in troughs in the data lines which represent phase formations. Primary Zn forms first in ZMA-2Sb at around 376 °C, which is approximately 15 °C above that of ZMA-0Sb, resulting in a higher liquidus. The solidus remains the same in both samples at just over 320 °C. The biggest difference displayed by these data is the absence of a binary eutectic formation curve in ZMA-2Sb, which confirms the removal of the phase as speculated during visual microstructure analysis above.

Full analysis of DSC testing can be seen in Table 3. Cooling formation data revealed a total rise in liquidus of 16.55 °C, increasing from 372.30 °C in ZMA-0Sb to 388.85 °C in ZMA-2Sb. The solidus remained constant at approximately 321–324 °C for all compositions. Solidification temperatures of the binary phase generally decreased, while the ternary eutectic formation temperature remained constant in all samples.

The morphology of Mg_3Sb_2 intermetallics was subsequently investigated using XRM. The imaging acquired through XRM resulted in a dataset containing eight separate intermetallics, identified as Mg_3Sb_2 . These can be seen clearly as flat, 2D structures of varying orientation, in Fig. 4. This is a representative volume to visualize the morphology of the intermetallics.

Table 4 shows the elemental composition as measured by EDX of each phase present in all four samples. As expected, the primary Zn phase has a consistent composition of around 99.2 wt% Zn, containing a maximum of 0.9% Al in solid solution. The binary and ternary eutectic phase are also consistent, with approximately 6.86% Mg-1.06% Al and 3.28% Mg-6.05%

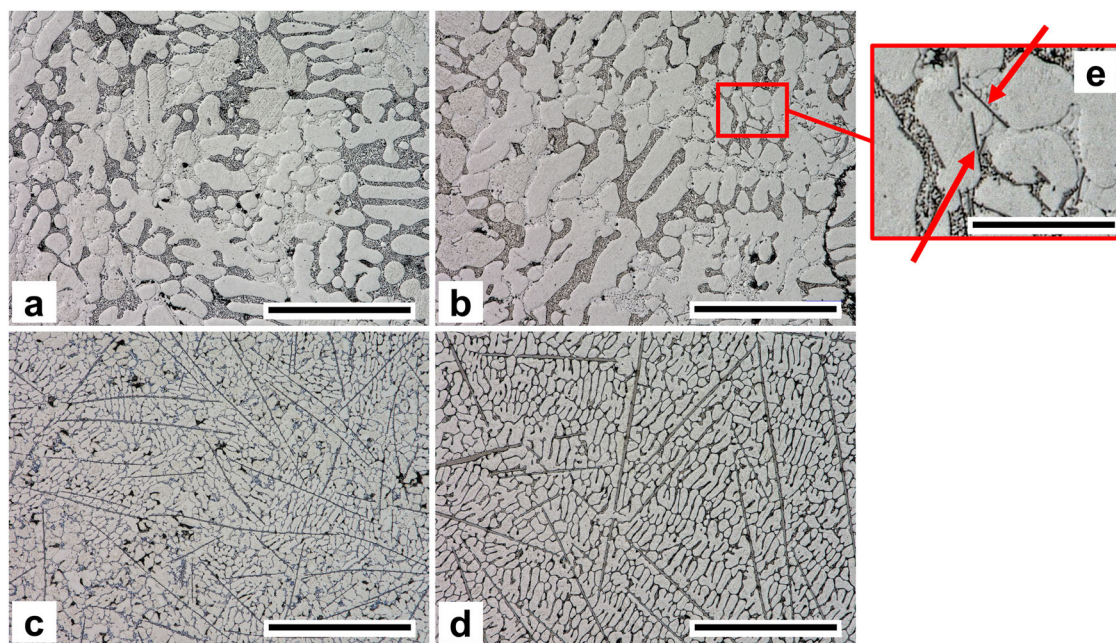


Fig. 1 | Optical micrographs of each sample. Each image was taken using a Keyence VHX-7000 showing **a** ZMA-0Sb, **b** ZMA-0.5Sb, **c** ZMA-1Sb, **d** ZMA-2Sb. A magnification box with annotations **e** shows the intermetallic needles more clearly for sample ZMA-0.5Sb. Scale bar of **a–d** is 200 μm . Scale bar of **e** is 50 μm .

Al in each phase, respectively. Due to their finer structure, EDX analysis was less reliable for Mg₃Sb₂ intermetallics, with a measured Sb content of between 61.5 and 74.8 wt%.

X-ray Photoelectron Spectroscopy was performed to investigate any changes to the surface oxide composition of the alloys that could subsequently impact their corrosion performance. The Zn auger spectrum data (Fig. 5) was used to confirm the composition of surface oxides, which showed only minor variations between samples. Peaks at approximately 986 eV and 989 eV are indicative of Zn oxides, while the presence of Zn metal is confirmed by peaks of 992 eV and 995 eV. Interestingly, the amount of Sb detected in the oxides appears to be very low, suggesting a negligible contribution to the air filmed oxide. These results were confirmed using an etching technique (Fig. 6), which show the atomic % of each element present as a function of etching time. As time, in this case, acts as a proxy for oxide thickness, the results are shown in terms of oxide depth, relative to the oxide/sample interface. This graph allows a comparison between the composition of the oxide and the same thickness of the bulk alloy. The results show a very similar oxide composition in both samples, consisting of Al₂O₃ and ZnO. The data confirms the negligible presence of Sb.

Electrochemical testing

False colour, time resolved maps of current density measured during SVET are shown in Fig. 7. ZMA-0Sb shows the initiation of two predominant anodic sites (shown in red) within the first hour of testing, while smaller areas continue to appear in approximately the same location after 6 h. A peak in current density of almost 5 Am⁻² was recorded across all samples tested, with a minimum of -3 Am⁻². As the weight percentage of Sb was increased, the number of anodic sites generally increased but decreased in intensity.

The average results from three open circuit potential tests and three linear polarisation resistance tests are shown in Fig. 8 and Fig. 9, respectively. OCP data showed a decrease of 12–17 mV for all three Sb addition samples when compared to the control (-0.999 mV). ZMA-0.5Sb displayed the most negative potential, averaging -1.018 mV between 4 and 24 hours.

Table 1 | Length and width measurements in μm for Mg₃Sb₂ intermetallic rods in samples ZMA0.5Sb and ZMA-2Sb

	ZMA-0.5Sb	ZMA-2Sb
Length (μm)	8.44	56.79
Width (μm)	0.45	1.59

This is followed by ZMA-1Sb and ZMA-2Sb, which average -1.014 mV and -1.013 mV between the same period, respectively. LPR showed an improvement in corrosion resistance with increasing Sb additions. Despite a constant increase in corrosion rate from 3.8 × 10⁻⁴ to 5.6 × 10⁻⁴ (Rp⁻¹) over 24 h, the average rate for ZMA-2Sb is considerably lower than the other

Table 2 | Phase area percentages in ZMA alloys with increasing Sb additions

Sample	Surface Area (%)			
	Primary Zn	Binary Eutectic	Ternary Eutectic	Mg ₃ Sb ₂ Intermetallic
ZMA-0Sb	56.2 (0.7)	13.8 (1.7)	24.2 (2.5)	0.0 (0.0)
ZMA-0.5Sb	60.0 (1.3)	5.0 (0.9)	23.6 (3.2)	0.9 (0.3)
ZMA-1Sb	60.0 (1.1)	4.4 (0.3)	20.8 (1.3)	4.4 (0.9)
ZMA-2Sb	71.4 (1.4)	Not detected	21.4 (2.3)	4.8 (0.5)

Standard deviation is given in brackets.

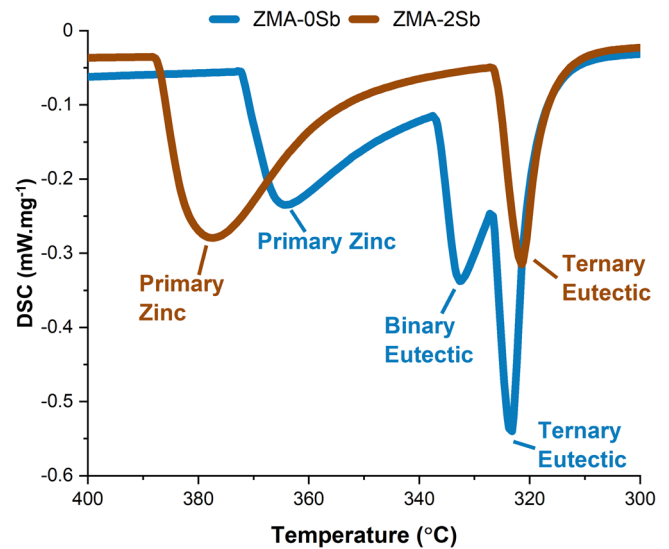


Fig. 3 | DSC cooling graph comparison for ZMA-0Sb and ZMA-2Sb samples. The graph shows no formation of binary eutectic with 2 wt% Sb additions.

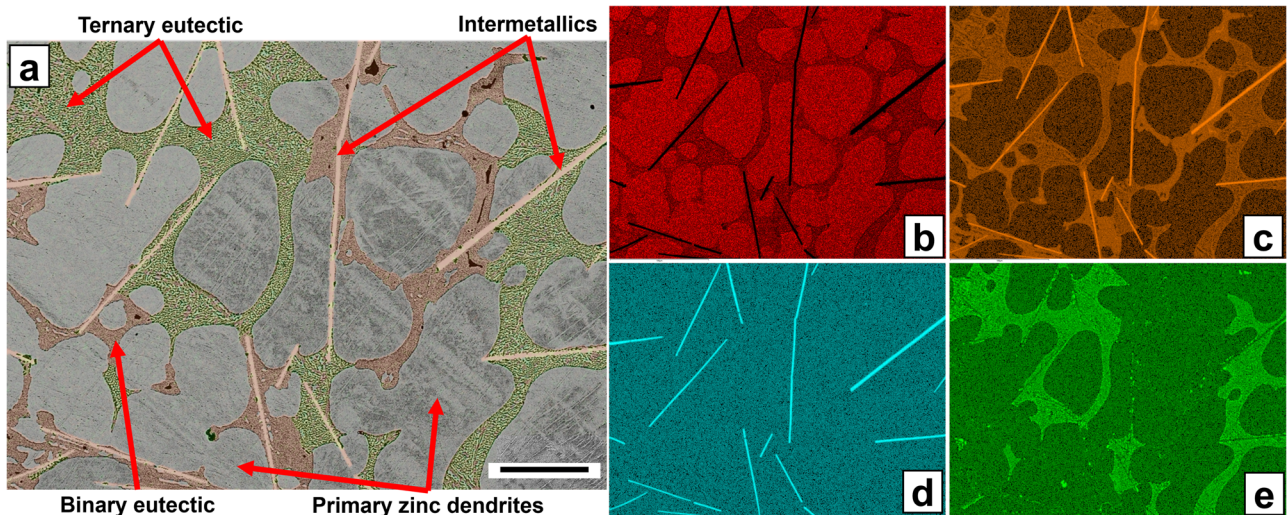


Fig. 2 | SEM and EDX images of ZMA-1Sb. a shows a false colour SEM image to provide greater contrast, with the binary eutectic phase highlighted in orange and the ternary eutectic phase in green. Separate EDX maps are shown in b Zn, c Mg, d Sb and e Al. Scale bar is 50 μm.

Table 3 | Averaged DSC data for the cooling of each sample

Sample	Cooling Formation Temperature (°C)			
	Primary Zn/ Liquidus	Binary Eutectic	Ternary Eutectic	Solidus
ZMA-0Sb	372.30 (0.00)	337.45 (0.05)	326.90 (0.10)	323.45 (0.15)
ZMA-0.5Sb	385.70 (0.20)	334.00 (0.20)	326.70 (0.20)	323.70 (0.20)
ZMA-1Sb	381.00 (0.00)	332.90 (0.40)	325.70 (0.40)	322.10 (0.30)
ZMA-2Sb	388.85 (0.25)	Not detected	326.95 (0.05)	321.35 (0.05)

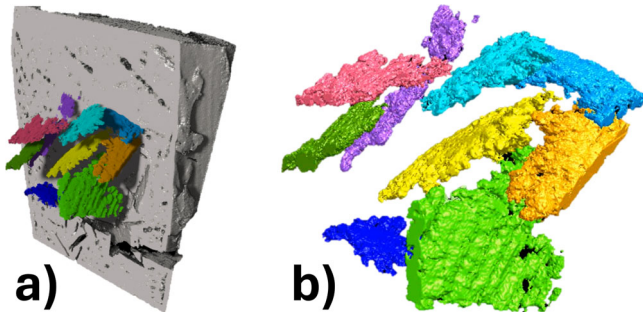


Fig. 4 | XRM false-colour imaging of ZMA-2Sb. **a** shows a section view of ZMA-2Sb with intermetallics highlighted in different colours, **b** shows intermetallic plates extracted from the ZMA-2Sb sample. The full height of the sample used, as shown in **a**, is 500 µm.

Table 4 | Phase composition within each sample

Sample	Phase	Element (wt%)			
		Zn	Mg	Al	Sb
ZMA-0Sb	Primary Zn	99.2 (0.1)	0	0.8 (0.1)	0
	Binary Eutectic	92.4 (0.2)	6.6 (0.1)	1.1 (0.1)	0
	Ternary Eutectic	90.7 (0.9)	3.2 (0.1)	6.1 (1.0)	0
ZMA-0.5Sb	Primary Zn	98.7 (0.4)	0	0.9 (0.1)	0
	Binary Eutectic	92.0 (0.1)	6.9 (0.1)	1.0 (0.1)	0
	Ternary Eutectic	90.4 (0.8)	3.3 (0.2)	5.7 (0.6)	0
	Mg ₃ Sb ₂ Intermetallic	17.6 (2.3)	19.5 (2.5)	0.1 (0.3)	61.5 (1.0)
ZMA-1Sb	Primary Zn	98.9 (0.1)	0	0.9 (0.0)	0
	Binary Eutectic	91.7 (0.2)	7.1 (0.2)	1.1 (0.1)	0
	Ternary Eutectic	90.7 (1.9)	3.6 (0.3)	5.1 (0.6)	0
	Mg ₃ Sb ₂ Intermetallic	3.4 (0.6)	20.6 (0.4)	0.1 (0.2)	74.8 (1.1)
ZMA-2Sb	Primary Zn	99.1 (0.1)	0.1 (0.1)	0.8 (0.0)	0
	Binary Eutectic	Not detected			
	Ternary Eutectic	89.6 (2.1)	3.02 (0.3)	7.28 (1.8)	0
	Mg ₃ Sb ₂ Intermetallic	15.9 (5.1)	18.2 (1.2)	0	65.4 (4.5)

Standard deviation is given in brackets

samples with an average R_p^{-1} value of 5.0×10^{-4} over 24 hours. ZMA-0Sb had the highest corrosion rate at 8.8×10^{-4} , with ZMA-0.5Sb and ZMA-1Sb averaging 7.4×10^{-4} and 7.7×10^{-4} , respectively. Cathodic polarisation showed that the cathodic current decreased by one order magnitude in the potential range -1.3 to -1.4 V compared to ZMA-0Sb, with ZMA-0.5Sb giving the best improvement compared to the control sample (Fig. 10). Anodic polarisation (Fig. 11) initially showed very little difference between samples. However, further analysis of data at approximately -1.006 V shows a small region of pseudo passivity in Sb samples compared to the

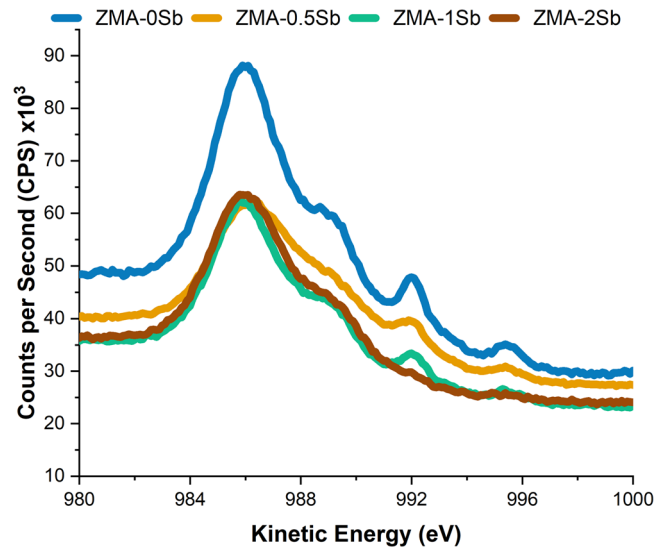


Fig. 5 | XPS test results. Kinetic energy in eV is shown on the x-axis and counts per second on the y-axis.

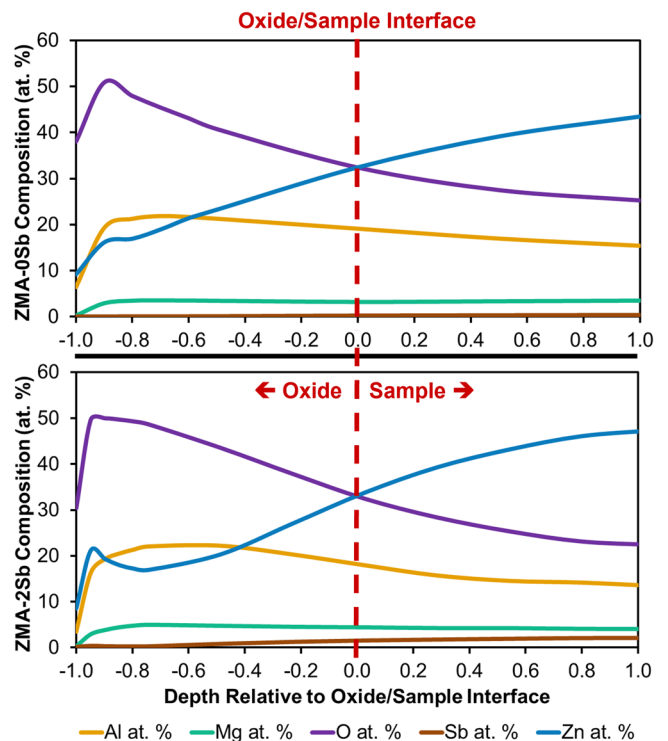


Fig. 6 | XPS etching composition data in at.%. Depth of the composition relative to the oxide surface (-1.0) is shown on the x-axis, where '0' is the oxide/sample interface. The results show negligible levels of Sb in both sample oxides.

control current of 2.25×10^{-5} A cm^{-2} . ZMA-0.5Sb, ZMA-1Sb and ZMA-2Sb have currents of 1.51×10^{-5} , 0.95×10^{-5} and 0.68×10^{-5} , respectively.

Figure 12 gives a comparison between samples at various times during TLM. Anodes in all three samples are established within 6 min of testing (shown as dark regions), with steady growth continuing in ZMA-0Sb and ZMA-0.5Sb. Zn-based corrosion product precipitation is observed as a ring at a distance from the anode representative of the chemical conditions in solution (ionic concentration and pH) whereby the solubility product of the corrosion product has become exceeded. Growth of anodes in ZMA-2Sb is

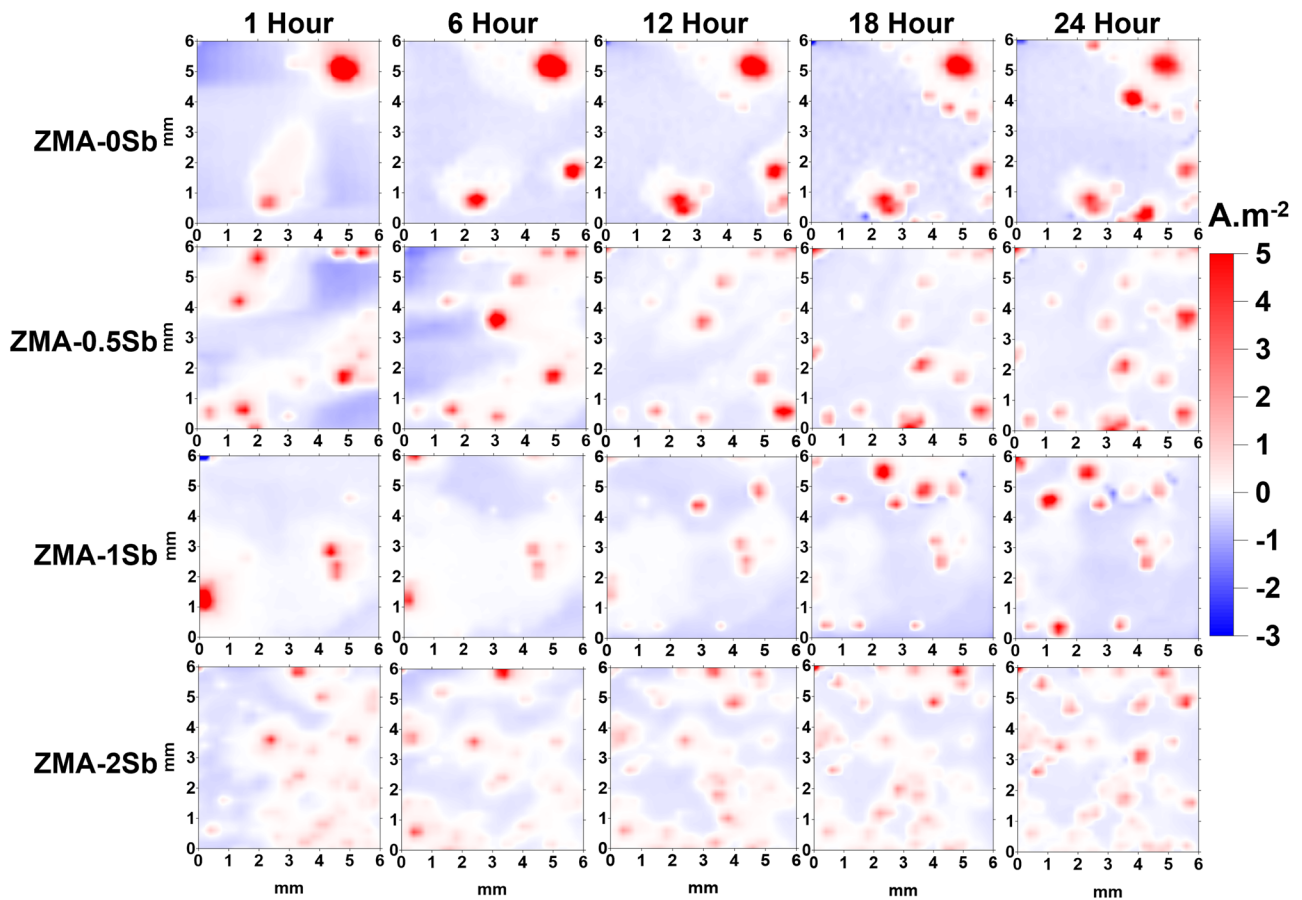


Fig. 7 | SVET maps for all four samples, using 1 wt% NaCl electrolyte solution at pH 7.0. Anodic behaviour is shown in red with a maximum of 5 A m^{-2} and cathodic behaviour is shown in blue with a maximum of -3 A m^{-2} .

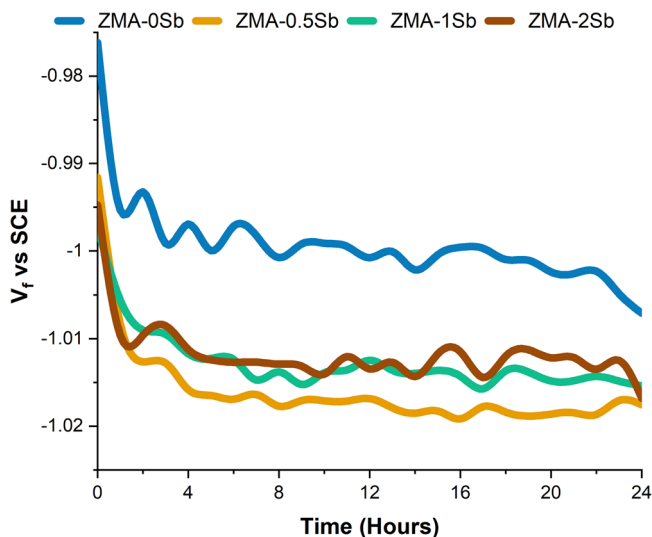


Fig. 8 | Averaged OCP data. The data shows a slight reduction in potential for ZMA alloys with Sb additions in 1 wt% NaCl electrolyte solution at pH 7.0.

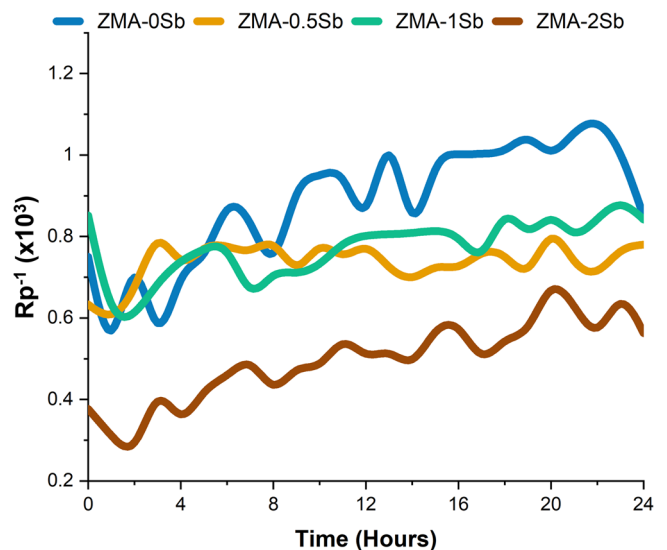


Fig. 9 | Averaged LPR data. The data shows that Sb additions to ZMA alloys produced a reduction in corrosion rate in 1 wt% NaCl electrolyte solution at pH 7.0.

slightly different however, where the multiple anodes present appear to reach their maximum size within the first 60 min. After this, trans-propagation of the anode takes place, spreading to adjacent areas on the sample surface.

To further investigate the effect of Sb on the corrosion mechanism at the microstructural level, the experiment was repeated using the master

alloy ZMA-4.8Sb at higher magnifications. These data can be seen in Fig. 13. Anodes initiate from a scratch on the sample surface (image a) and continue to grow across the primary Zn phase dendrites. Images b, c and d show the growth behaviour of the anode as it is halted by the presence of Mg_3Sb_2 intermetallics within the microstructure (identified in red) and continues

instead along the primary Zn, perpendicular to the length of the intermetallics.

Discussion

The addition of Sb to ZMA alloy resulted in the precipitation of an Sb-rich quaternary phase. The formation of Mg_3Sb_2 intermetallics, which solidify initially at 1227 °C²¹, were confirmed by SEM and EDX. Furthermore, XRM was used to characterise the morphology of the Sb rich phases as flat disk shapes, which is contrary to findings in earlier publications^{22,23} where they are described as 'needles'. An increase in Sb additions from 0.5 wt% to 2 wt% caused an increase in the length and width of the intermetallics, an effect also seen in the addition of Sb to Mg alloys²⁴. The use of DSC and microscopy on ZMA-1Sb confirmed the subsequent formation of primary Zn phase ($Zn_{99.2}-Al_{0.8}$) at approximately 381.0 °C, which nucleates from the Mg_3Sb_2 intermetallics. This is followed by the binary and ternary eutectics at 332.9 °C and 325.7 °C, respectively. Figure 1 also shows an apparent

decrease in Zn dendrite size as Sb is increased, leading to a more refined microstructure.

Increasing the Sb additions in the ZMA alloy leads to a wider solidification temperature range, increasing the liquidus due to a shift away from the eutectic composition towards the Zn-rich part of the phase diagram. This is caused by the rise in proportion of Mg_3Sb_2 , thereby reducing the amount of free Mg that is available. Microscopy and DSC results concluded a complete elimination of the binary eutectic phase in ZMA-2Sb. An increase in Mg_3Sb_2 intermetallics reduces the proportion of Mg available in solution at solidification, restricting growth of the binary. Instead, the solidification of the ternary eutectic became more thermodynamically favourable.

The addition of Sb to this ZMA has an appreciable effect on the corrosion behaviour of the alloy and this is thought to be due to the modifications to the microstructure induced by Sb. The control ZMA-0Sb displayed anodic behaviour typical of these alloys, with preferential attack of the binary and ternary eutectic phases due to the presence of $MgZn_2$ ²⁵⁻²⁷. Therefore, as the binary eutectic volume fraction is reduced with increasing Sb levels from 13.8% (ZMA-0Sb) to 0% (ZMA-2Sb), the anodic attack becomes increasingly restricted to the ternary eutectic. The microstructure additionally is refined with increasing Sb additions, as shown in Fig. 1, and hence the propagation of anodes becomes restricted, and anodes initiate at more sites over the sample area as observed in Fig. 7.

The electrochemical data regarding OCP and LPR presented in Figs. 8 and 9 show that 0.5 wt% Sb additions led to a reduction in potential with respect to the control alloy and a decrease in the corrosion kinetics. Sb additions up to 2 wt% further reduced the corrosion rate but shifted the potential anodically with respect to ZMA-0.5Sb (but remained more negative than the control ZMA-0Sb). These shifts in potential and kinetics are best explained through consideration of schematic Evans diagrams and examination of the quantitative microstructural changes within the alloys. Considering Fig. 14a, d, an idealised Evans diagram and schematic of the microstructure for ZMA-0Sb is presented. Here, the alloy adopted a free corrosion potential of E_{0Sb} and a free corrosion current of i_{0Sb} . The microstructure was composed of Zn dendrites along with binary and ternary eutectics as described in Section 2.1. The addition of 0.5Sb caused a cathodic shift in potential to $E_{0.5Sb}$ with a subsequent reduction in corrosion kinetics to $i_{0.5Sb}$, as shown in Fig. 14b for ZMA-0.5Sb. As such, the system was cathodically deactivated as highlighted by the cathodic polarisation data in Fig. 10. The anodic kinetics were also reduced as shown in Fig. 11 but the net dominating effect is one of cathodic deactivation. This will be discussed later.

The addition of 0.5Sb leads to a significant decrease (8.8%) in binary eutectic and the formation of 0.9% area fraction of the Mg_3Sb_2 intermetallic phase. The Zn dendrite surface area fraction increased to 60% while the ternary eutectic remained fairly constant (23.6%). This is schematically presented in Fig. 14e. Time lapse microscopy showed anodic events initiated adjacent to but not on the Mg_3Sb_2 intermetallics and anodes progressed until they reached another intermetallic where their progress was halted. This suggests the Mg_3Sb_2 intermetallics were cathodic with respect to the metal matrix and anodes initiated locally to them via galvanic coupling, which is supported by the reported Sb reduction potential of 0.21 V²⁸. This is different to 0Sb ZMA alloys, where the Zn dendrites act as the cathode. Post corrosion imaging showed no damage to the Mg_3Sb_2 intermetallics, further supporting the idea that these were cathodic with respect to the bulk alloy. Therefore, the Mg_3Sb_2 phase acts cathodically in the alloy and the drop in OCP (Fig. 8) and corrosion rate (Fig. 9) suggests that the kinetics of cathodic activity are lower for Mg_3Sb_2 than phases in the control alloy and hence, the overall corrosion kinetics decrease due to cathodic deactivation. This is further supported by the one order of magnitude decrease in cathodic kinetics in the diffusion-limited oxygen reduction region of the cathodic polarisation curve for ZMA-0.5Sb in Fig. 10.

Higher additions of Sb to 2 wt% subsequently led to an anodic shift in potential to E_{2Sb} with respect to $E_{0.5Sb}$ (although the potential was still cathodic with respect to the control E_{0Sb}) and a further decrease in corrosion

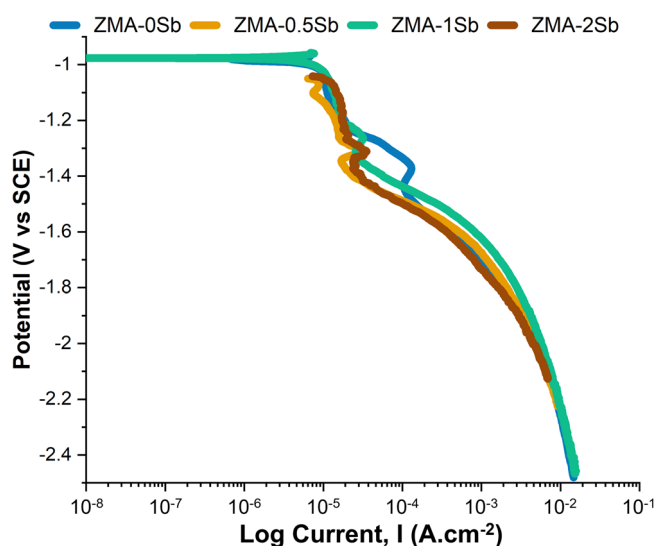


Fig. 10 | Cathodic polarisation data of ZMA alloys. Sb addition samples show a reduced cathodic current in comparison to the control between -1.3 V and -1.4 V in 1 wt% NaCl electrolyte solution at pH 7.0.

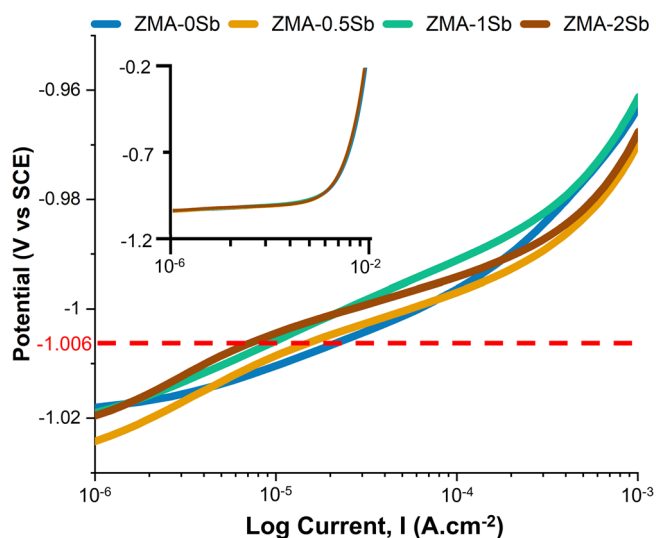
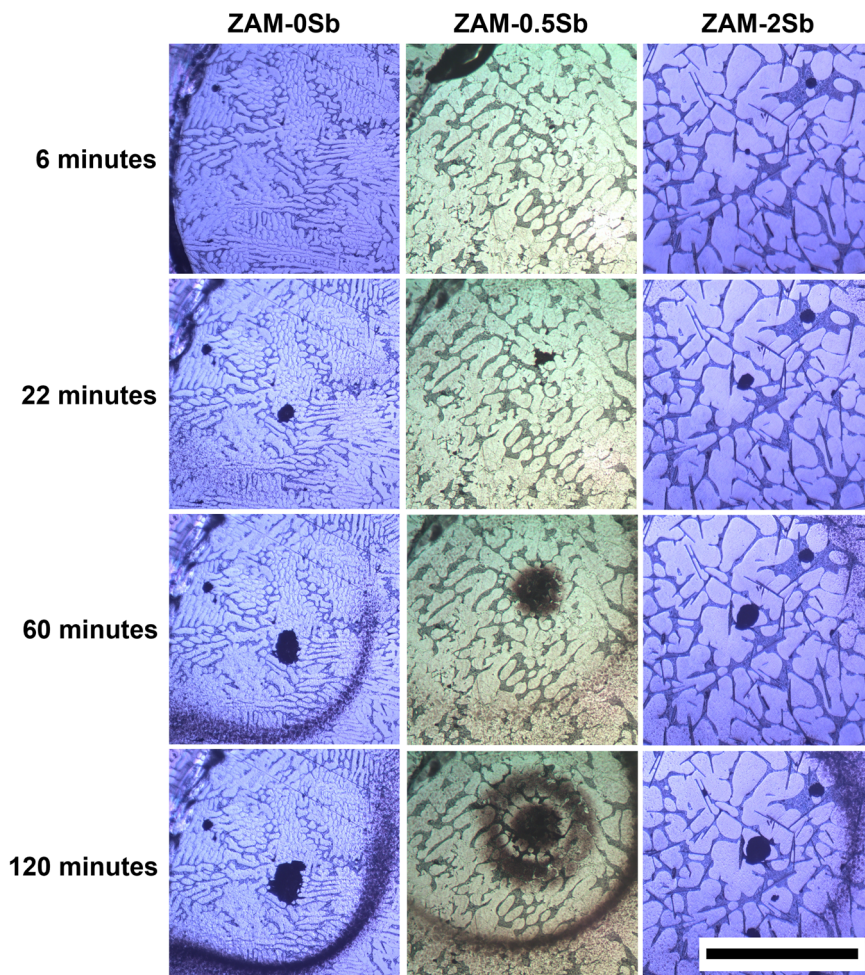


Fig. 11 | Anodic polarisation data of ZMA alloys. Sb addition samples show reduced anodic current in comparison to the control between -0.95 V and -1.03 V in 1 wt% NaCl electrolyte solution at pH 7.0. Inset graph shows the full data range from -0.2 V to -1.2 V, with very little change between samples.

Fig. 12 | Comparison of ZMA-Sb samples at 6, 22, 60 and 120 min during TLM testing. Testing was carried out in 1 wt% NaCl electrolyte solution at pH 7.0. Scale bar is 500 μm .



current to $i_{2\text{Sb}}$ represented in Fig. 14c. This reflects the increase in OCP observed for ZMA-2Sb in Fig. 8 but the further reduced corrosion rate as shown in Fig. 9.

The net cathodic deactivation of the system once again resulted from the presence of the Mg_3Sb_2 intermetallic phase. However, considering Fig. 10, it seems that the reduction in cathodic currents in the diffusion-limited current region of oxygen reduction are non-linear with respect to increasing Sb additions. Therefore, even low volume fractions of Mg_3Sb_2 are sufficient to reduce the cathodic kinetics of the system possibly due to the reported reduction potential of Sb of 0.21 V. Any further subsequent reductions in cathodic current with increasing levels of Mg_3Sb_2 may possibly be limited by other changes to the microstructure, particularly the increase in primary Zn volume fraction (56.2% to 71.4%) that can also support cathodic activity.

However, as stated, ZMA-2Sb displayed a concurrent anodic deactivation mechanism shown by the increase in potential with respect to ZMA-0.5Sb (Fig. 8) but decrease in corrosion rate with respect to the control (Fig. 9). As stated prior, the anodic dissolution mechanism in the control system is preferential attack of the MgZn_2 present in the binary and ternary eutectic phases. This is due to the low free corrosion potential of MgZn_2 of -1.2 V vs SCE. With increasing Sb additions, the binary eutectic surface area fraction is reduced and ultimately removed from the structure in ZMA-2Sb and hence the overall eutectic volume fraction of MgZn_2 (binary + ternary) is reduced as Mg is sequestered into the Mg_3Sb_2 phase as shown schematically in Fig. 14f. Therefore, the amount of available Mg to participate in the anodic reaction is reduced leading to the decrease in anodic current observed in Fig. 11 and thus, a decreased corrosion rate of the alloy. Additionally, the ternary eutectic contains Al rich nodules that will have an alumina air-formed film oxide that could offer a level of pseudo passivity to the eutectic phase as

observed in the anodic polarisation curves. Therefore, the amount of the most anodically susceptible phase has been reduced in the microstructure and so anodic deactivation is observed. The Mg has now preferentially formed Mg_3Sb_2 and as such its presence in the microstructure has changed from that of an anodically susceptible phase to a cathodically susceptible phase with poor cathodic kinetics and hence the corrosion rate of the alloys with Sb additions are reduced.

The density of Mg_3Sb_2 was calculated to be (4.03 g cm^{-3}), which is lighter than liquid Zn (6.62 g cm^{-3}). It is therefore likely that particles will rise to the top of the galvanising bath and be removed with dross. Additionally, an increase in the freezing range shown through DSC is likely to make wiping during bath withdrawal difficult. The addition of Sb to ZMA coatings is therefore unsuitable for continuous galvanising but could be investigated for use in sacrificial anodes for marine applications.

Methods

Sample production

The samples were produced by adding 40 g of Sb rod (99.999% pure) to 800 g of ZMA base alloy containing 1–2 wt% Al and Mg. This was heated to 840°C in a crucible melting furnace for 18 h and splat cast onto an 8 mm thick copper plate to simulate the rapid cooling seen in a galvanising line. The master alloy composition was measured to be 4.8 wt% Sb. This was then diluted by adding ZMA to give the compositions shown in Table 5. A control with no Sb additions was produced using the same heating method. The composition of all samples used in this study were confirmed by Inductively Coupled Plasma Optical Emission Spectroscopy (ICP-OES) with an accuracy of 1 ppm.

Fig. 13 | TLM optical microscope images of ZMA-4.8 Sb. TLM microscope images of ZMA-4.8 Sb at **a** 100 min, **b** 140 min, **c** 220 min, **d** 440 min. The images show anode growth in 1 wt% NaCl electrolyte solution at pH 7.0. Scale bar is 100 μm .

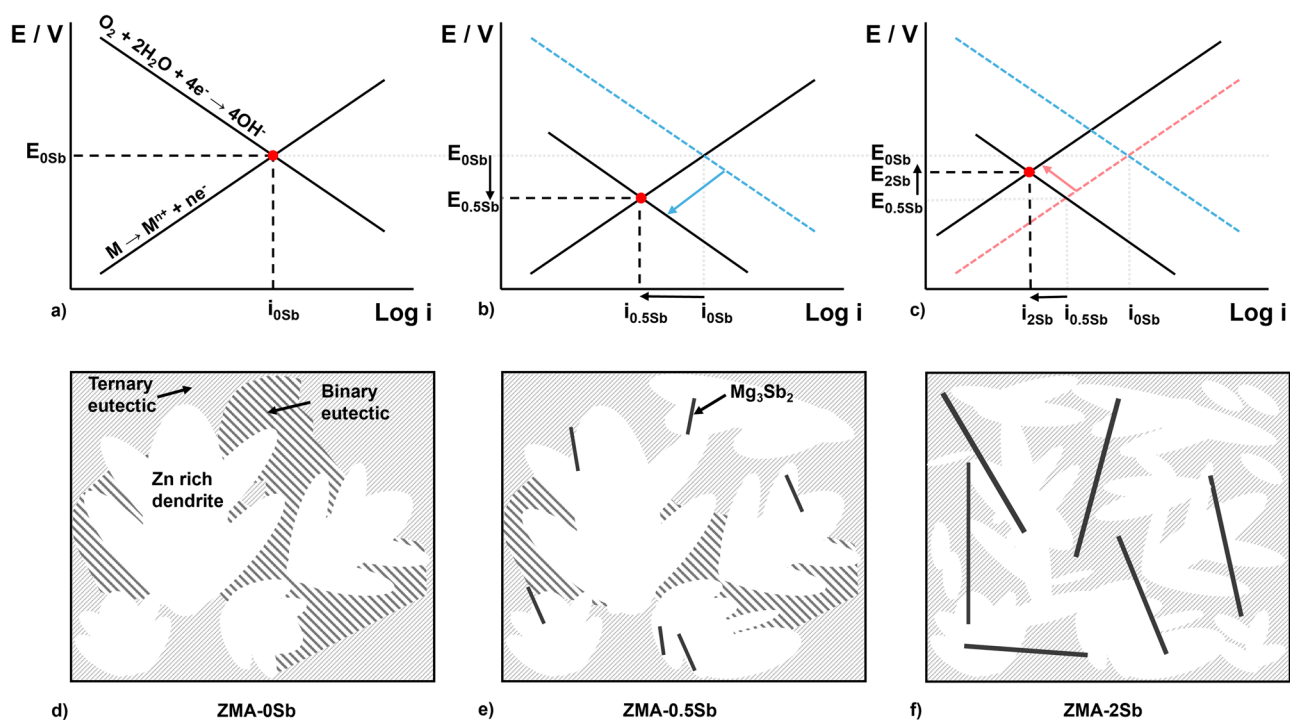
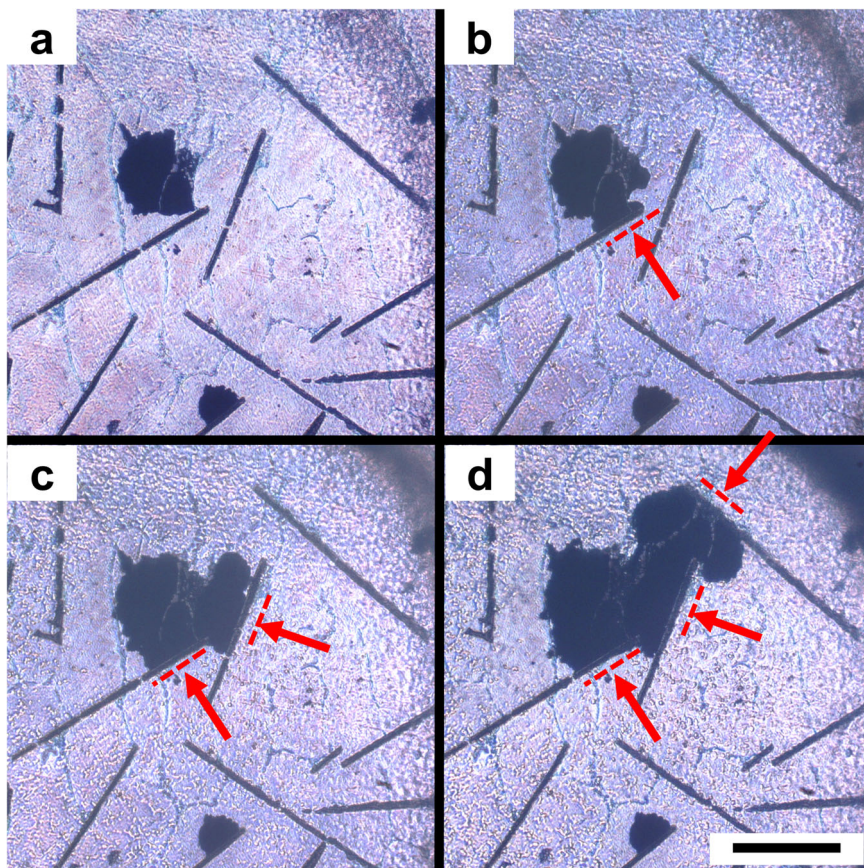


Fig. 14 | Schematics to provide an explanation of corrosion behaviour. Evans diagrams (a–c) and microstructure schematics (d–f). The diagrams provide a visual explanation of corrosion behaviour.

Table 5 | Addition of Sb to each sample, in wt%, measured using ICP-OES

Sample	Sb wt% Addition
ZMA-0Sb	<0.01
ZMA-0.5Sb	0.45
ZMA-1Sb	0.83
ZMA-2Sb	1.80

Phase confirmation

Each sample was mounted in conductive resin and progressively ground to a surface finish 0.2 μm . Etching was performed using a 2% Nital solution for 8 s, followed by rinsing with ethanol. Microstructure images were captured using a Zeiss Evo LS25 Scanning Electron Microscope (SEM) with an Oxford Instruments X-MaxN 50 Energy Dispersive X-ray Spectroscopy (EDX) module, as well as a Keyence VHX-7000 optical microscope. Phase area percentage was calculated using five images, randomly obtained from each sample. Phase composition was taken as an average of five EDX single-point scans per sample.

Mg_3Sb_2 intermetallic measurements were obtained by taking three low-magnification and three high-magnification images of sample microstructures, each randomly placed. Each intermetallic was measured manually with Image Pro 10 software and an average taken. The Keyence microscope's in-built grain analysis tool was used for phase proportions.

Differential scanning calorimetry

A Netzsch STA 449 F1—High-Temperature DSC was used to determine the phase transformations and liquidus/solidus temperatures of the ZMA material by detecting heat flow between the sample and an alumina reference crucible. The on-set temperatures were detected using Netzsch Proteus software by using the secondary differential inflection point of the phase transitions. The heating and cooling rates used were 10 k min^{-1} . All experiments were performed under argon cover gas. The average of two DSC tests was used to analyse the phase transformations present within each alloy composition when cooled from 450 $^\circ\text{C}$.

X-ray photoelectron spectroscopy

X-Ray photoelectron spectroscopy (XPS) was performed on a Kratos Axis Supra instrument using a monochromated Al K_α x-ray source with 15 mA emission current and 225 W power. A minimum of three survey scans with a pass energy of 160 eV were collected for each sample to confirm the elements present on the surface. Subsequently high-resolution spectra of the surface were collected at a pass energy of 40 eV, with the x-ray spot size an oval of $\sim 300 \times 700\ \mu\text{m}$. The conductive substrate negated the need for charge neutralisation. Where charge correction was required, it was to the hydrocarbon line of adventitious carbon at 284.8 eV. Spectra were quantified using CasaXPS (Version 2.3.24PR1.0) using the Kratos sensitivity factor library. Due to the overlap of the O(1s) & Sb(3d) regions, quantification required modelling with synthetic components—the Sb(oxide) $3d_{5/2}$ peak is wholly obscured by the O(1s), but otherwise the Sb(metal) and Sb(oxide) $3d_{3/2}$ peaks are unobscured.

X-ray microscopy

Analysis of the ZMA alloys via X-ray microscopy (XRM) was achieved using a lab-based Zeiss Xradia Versa 520 X-ray Microscope using a CCD detector system with scintillator-coupled visible light optics and tungsten transmission target. Specimen cross sections of between 1000 and 500 μm were imaged, with varying X-ray parameters to enable visualization of the phases within the material. An X-ray tube voltage of 140 kV and a current of 71 μA was used, with an exposure of 22,000 ms and a total of 3201 projections captured over a 360-degree range. An objective lens giving an optical magnification of 20 \times was selected with binning set to 2, producing isotropic voxel (3-D pixel) sizes of 0.505 μm . A high energy filter was placed in the

beam path (HE2 – proprietary Carl Zeiss microscopy filter). The tomograms were firstly reconstructed as 16-bit from 2-D projections using a Zeiss commercial software package (XMReconstructor, Carl Zeiss), a cone-beam reconstruction algorithm based on filtered back-projection. XMReconstructor was also used to produce 2-D grey scale slices for intermediate analysis.

A new method of artificial intelligence tomogram reconstruction was used that has the potential to improve upon the filtered back-propagation method. The machine learning (ML)-based DeepRecon (Carl Zeiss Microscopy) software was used to reconstruct the data from the raw projection, which produced slightly greater contrast between the Mg_3Sb_2 intermetallics and the other phases, giving greater confidence in subsequent segmentation potential. Further machine learning methods were used to segment the Mg_3Sb_2 structures (Intellisis software, Carl Zeiss) which involved manually 'tagging' each phase within a sampled internal region of interest (ROI), typically colouring a few slices, which were used as the training data for the ML model.

Human intervention was then used to validate the segmentation compared to the visible greyscale XRM data.

Corrosion studies

All corrosion study samples used were mounted in a non-conductive resin and prepared in the same way used for microstructural analysis except for etching. The surface of all test samples was masked off using 3 M non-conductive PTFE tape and a 1 mm diameter biopsy pen. A piece of tape was then removed from the middle of the sample to give a working area of 36 mm^2 for OCP, LPR, SVET, and polarisation tests, and 0.78 mm^2 for TLM. A Gamry Interface 1010E Potentiostat was used for data capture. The electrolyte used for all tests was 1 wt% aqueous NaCl with a pH of 7.0, at room temperature, with an assumed constant dissolved oxygen concentration of $2.8 \times 10^{-4}\ \text{mol dm}^{-3}$ 29.

Scanning vibrating electrode technique

The scanning vibrating electrode technique (SVET) is used to obtain semi-quantitative, comparable corrosion data from metallic samples and can resolve spatial and temporal information about a metal corroding in solution. SVET achieves this by vibrating a glass-enclosed platinum wire micro-tip probe of 125 μm diameter normal to the sample surface at a constant frequency of 140 Hz, amplitude of 25 μm and height of 100 μm . As the sample corrodes freely in the aqueous electrolyte, an ionic current flux occurs between the anodic and cathodic regions of the sample surface. As the electrolyte has a finite resistivity the passage of the ionic current flux creates lines of iso-potential within the electrolyte. The SVET probe thus detects a potential gradient in solution that is directly proportional to the ionic current flux and there the location and intensity of anodes and cathodes can be determined spatially and temporally. The advantages and limitations of SVET, as well as previously established instrument design and operating procedure can be found here^{30–33}. During SVET testing, 31 measurements along the x and y-direction were made, generating 961 data points for each scan. One scan was taken every hour for 24 h and three repeat tests were carried out for each sample.

SVET calibration was carried out using a two-compartment cell which each contained a platinum electrode and were joined by a vertically positioned glass tube. The SVET tip was placed within the glass tube and exposed to different currents using a nano-galvanostat. Lines of current flux were aligned vertically along the length of the tube, which allowed the SVET tip to be vibrated in an environment of uniform current density, independent of probe height. By plotting a gradient of current density vs SVET voltage in 'Surfer' software, a calibration factor could be found and applied to the SVET apparatus.

Time lapse microscopy

Time lapse microscopy (TLM) allows the corrosion of a metallic surface to be viewed clearly under magnification at a microstructural level while in the

presence of an aqueous electrolyte. Still images are captured periodically over a set length of time and stitched together to form a video. This method allows the anodic and cathodic behaviour of corrosion to be visualised over a relatively large area of material. Previous methodologies are detailed in former publications^{16,29,34}. TLM samples were secured to the base of a petri dish using double-sided tape and immersed in 250 mL of electrolyte. Images were taken every 2 min with a Meiji Techno 7100 optical microscope with an Infinity 2 digital camera attachment, for a total time of 24 h. These images were converted into a 36 s video with the help of movie maker software. One second of finished video therefore equates to 40 minutes of image acquisition.

Open circuit potential and linear polarisation resistance

OCP and LPR testing were both carried out by completely immersing the samples in electrolyte and connecting an insulated electrode to the rear of the corroding surface. A 1 cm² platinum counter electrode and a saturated calomel reference electrode (SCE) were also immersed within the electrolyte. The OCP measurements were conducted for 24 h using a 2-electrode setup. LPR measurements were conducted using a 3-electrode set-up. Methodologies are explained further in previous publications^{35,36}.

Anodic and cathodic polarisation

Potentiodynamic scans were initiated at 150 mV below the OCP scanning in the positive direction for the anodic curve and 150 mV above the OCP scanning in the negative direction for the cathodic curve, both at a rate of 0.166 mV s⁻¹. Anodic and cathodic sweeps were measured independently on fresh samples. Measurements were initiated as soon as the electrolyte was introduced. All the electrochemical data presented are the mean values of three experiments.

Received: 29 February 2024; Accepted: 23 May 2024;

Published online: 07 June 2024

References

- Marder, A. R. The metallurgy of zinc-coated steel. *Prog. Mater. Sci.* **45**, 191–271 (2000).
- LeBozec, N. et al. Corrosion performance of Zn–Mg–Al coated steel in accelerated corrosion tests used in the automotive industry and field exposures. *Mater. Corros.* **64**, 969–978 (2013).
- Zhang, X., Leygraf, C. & Wallinder, I. O. Atmospheric corrosion of Galfan coatings on steel in chloride-rich environments. *Corros. Sci.* **73**, 62–71 (2013).
- Berkhout, B. Dane, C. Advanced zinc coatings for improved performance and press shop efficiency. Proc. 5th International Conference on Steels in Cars and Trucks. Amsterdam, Netherlands (2017).
- Wang, T., Zhao, M., Li, Z., Wang, X. & Wei, J. Effect of indium on the microstructure and corrosion resistance of the galvanising coating. *Mat. Sci. Tech.* **39**, 767–776 (2023).
- Bracka-Kesek, K., Szczyzny, A., Guzik, E. & Kopycinski, D. Evaluation of effect of Ti addition to zinc bath on kinetics of growth of alloy layer formed in process of hot-dip galvanisation on steel substrate. *Mater* **16**, 4773 (2023).
- Dong, A. et al. Effect of Mg on the microstructure and corrosion resistance of the continuously hot-dip galvanizing Zn–Mg coating. *Mater* **10**, 980 (2017).
- Schuerz, S. et al. Corrosion behaviour of Zn–Al–Mg coated steel sheet in sodium chloride-containing environment. *Corros. Sci.* **51**, 2355–2363 (2009).
- Prosek, T. et al. Effect of the microstructure of Zn–Al and Zn–Al–Mg model alloys on corrosion stability. *Corros. Sci.* **110**, 71–81 (2016).
- Vlot, M. et al. Hot Dip ZnAlmg Coatings: Microstructure And Forming Properties. Proc. 7th International Conference on Zinc and Zinc Alloy Coated Steel Sheet. Osaka, Japan (2007).
- Pesci, C. et al. ZM coatings: a complementary offer sustaining weight-lightening. Proc. 5th International Conference on Steels in Cars and Trucks. Amsterdam, Netherlands (2017).
- Malla, A. et al. Zinc Alloy coatings thickness and effect on performance. Proc. 112th Meeting of Galvanizer's Association. South Carolina, USA (2022).
- Ahmadi, M., Salgin, B., Kooi, B. J. & Pei, Y. Genesis and mechanism of microstructural scale deformation and cracking in ZnAlMg coatings. *Mater. Des.* **186**, 1–15 (2020).
- Wint, N. et al. The kinetics and mechanism of filiform corrosion occurring on zinc-aluminium-magnesium coated steel. *Corros. Sci.* **158**, 108073 (2019).
- Guo, X. & He, G. Opportunities and challenges of zinc anodes in rechargeable aqueous batteries. *J. Mater. Chem. A.* **23**, 11987–12001 (2023).
- Wint, N. et al. The ability of Mg₂Ge crystals to behave as 'smart release' inhibitors of the aqueous corrosion of Zn–Al–Mg alloys. *Corros. Sci.* **179**, 109091 (2021).
- Chang, S. & Shin, J. C. The effect of antimony additions on hot dip galvanized coatings. *Corros. Sci.* **36**, 1425–1436 (1994).
- Paliwal, M. & Jung, I. Thermodynamic modeling of the Mg–Bi and Mg–Sb binary systems and short-range-ordering behavior of the liquid solutions. *Calphad* **33**, 744–754 (2009).
- Guide Chem, Magnesium Antimonide 12057-75-9. <https://www.guidechem.com/dictionary/en/12057-75-9.html> [Last accessed 20 December 2023].
- Li, B., Long, W. & Zhou, X. The effect of Ti on the microstructure and mechanical properties of (Ti+Mg₃Sb₂)/Mg composites. *Adv. Compos. Lett.* **29**, 1–8 (2020).
- Okamoto, H. Mg–Sb (Magnesium–Antimony). *J. Phase. Equilib. Diffus.* **31**, 574 (2010).
- Guangyin, Y., Yangshan, S. & Wenjiang, D. Effects of bismuth and antimony additions on the microstructure and mechanical properties of AZ91 magnesium alloy. *Mater. Sci. Eng. A.* **308**, 38–44 (2001).
- Guangyin, Y., Yangshan, S. & Wenjiang, D. Effects of Sb addition on the microstructure and mechanical properties of AZ91 magnesium alloy. *Scr. Mater.* **43**, 1009–1013 (2000).
- Balasubramani, N. et al. Effect of antimony addition on the microstructure and mechanical properties of ZA84 magnesium alloy. *J. Alloy. Compd.* **455**, 168–173 (2008).
- Wint, N. et al. The effect of microstructural refinement on the localized corrosion of model Zn–Al–Mg alloy coatings on steel. *J. Electrochem. Soc.* **166**, C3147–C3158 (2019).
- Cooze, N. et al. Effect of pH on the corrosion mechanism of zinc magnesium aluminium alloy coatings for steels. ECS. Meet. Abstr. 786 (2022).
- Diler, E. Characterization of corrosion products of Zn and Zn–Mg–Al coated steel in a marine atmosphere. *Corros. Sci.* **87**, 111–117 (2014).
- Lenntech, Antimony – Sb. <https://www.lenntech.com/periodic/elements/sb.htm> [Last accessed 28 February 2024].
- Kaye, G. W. C., Laby, T. H. Tables of Physical and Chemical Constants (15th ed.) 219–220 (Longman Publishing, 1986).
- Sullivan, J. et al. In situ monitoring of corrosion mechanisms and phosphate inhibitor surface deposition during corrosion of zinc-magnesium-aluminium (ZMA) alloys using novel time-lapse microscopy. *Faraday Discuss.* **180**, 361–379 (2015).
- Isaacs, H. S. The effect of height on the current distribution measured with a vibrating electrode probe. *J. Electrochem. Soc.* **138**, 722–728 (1991).
- Bastos, A. C., Quevedo, M. C., Karavai, V. & Ferreira, M. G. S. On the application of the scanning vibrating electrode technique (SVET) to corrosion research. *J. Electrochem. Soc.* **164**, 973–990 (2017).
- Bohm, S., McMurray, H. N., Powell, S. M. & Worsley, D. A. Photoelectrochemical investigation of corrosion using scanning electrochemical techniques. *Electrochim. Acta* **45**, 2165–2174 (2000).

34. Yoo, J. D. et al. The effect of an artificially synthesized Simonkolleite layer on the corrosion of electrogalvanized steel. *Corros. Sci.* **70**, 1–10 (2013).
35. Malla, A. D. et al. Mechanistic study on the corrosion behaviour of Zinc and Zinc-Calcium alloys designed for enhanced metallic coatings in the presence of chloride and phosphate ions. *Corros. Sci.* **213**, 110956 (2023).
36. Grech, I. S. et al. Evaluating the corrosion performance of wrought and additively manufactured (AM) Invar[®] and 17-4PH. Solid Freeform Fabrication Symposium. Texas, USA (2019).

Acknowledgements

We would like to thank both EPSRC and Tata Steel for their funding to the COATED Centre for Doctoral Training, as well as Swansea University's AIM facility, the SPECIFIC Pilot Manufacturing Research Centre and the MACH1 project.

Author contributions

D.A. Britton: Investigation, methodology, data curation, formal analysis, writing, review and editing. D. Penney: Conceptualization, methodology, validation, formal analysis, supervision, writing, review and editing. A.D. Malla: Investigation, methodology, data curation, formal analysis. S. Mehraban: Investigation, methodology, data curation, formal analysis. J. Sullivan: Methodology, validation, formal analysis, supervision, writing, review and editing. M. Goldsworthy: Investigation, data curation. J. McGettrick: Investigation, data curation, formal analysis. R. Johnston: Investigation, data curation, formal analysis. R.L. Mitchell: Investigation, data curation. C. Challinor: Supervision, review and editing.

Competing interests

The authors declare no competing interests.

Additional information

Supplementary information The online version contains supplementary material available at <https://doi.org/10.1038/s41529-024-00481-7>.

Correspondence and requests for materials should be addressed to Daniel A. Britton.

Reprints and permissions information is available at <http://www.nature.com/reprints>

Publisher's note Springer Nature remains neutral with regard to jurisdictional claims in published maps and institutional affiliations.

Open Access This article is licensed under a Creative Commons Attribution 4.0 International License, which permits use, sharing, adaptation, distribution and reproduction in any medium or format, as long as you give appropriate credit to the original author(s) and the source, provide a link to the Creative Commons licence, and indicate if changes were made. The images or other third party material in this article are included in the article's Creative Commons licence, unless indicated otherwise in a credit line to the material. If material is not included in the article's Creative Commons licence and your intended use is not permitted by statutory regulation or exceeds the permitted use, you will need to obtain permission directly from the copyright holder. To view a copy of this licence, visit <http://creativecommons.org/licenses/by/4.0/>.

© The Author(s) 2024